Nanoprecipitation in a Beta-Titanium Alloy

James Coakley[a,*], Vassili A Vorontsov[a], Kenneth C Littrell[b], Richard K Heenan[c], Masato Ohnuma[d], Nicholas G Jones[e], David Dye[a]

[a] *Department of Materials, Imperial College, South Kensington, London SW7 2AZ, England*
[b] *Oak Ridge National Laboratory, Chemical and Engineering Materials Division, Oak Ridge, TN 37831, USA*
[c] *Rutherford Appleton Laboratory, Didcot, Oxon OX11 0QX, England*
[d] *Laboratory of Quantum Beam System Engineering, Hokkaido University, Sapporo 060-0808, Japan*
[e] *Department of Materials Science and Metallurgy, University of Cambridge, Cambridge CB2 3QZ, England*

Abstract

This paper represents the first application of small angle neutron scattering (SANS) to the study of precipitate nucleation and growth in β-Ti alloys in an attempt to observe both the precipitation process *in-situ* and to quantify the evolving microstructure that affects mechanical behaviour. TEM suggests that athermal ω can be induced by cold-rolling Gum metal, a β-Ti alloy. During thermal exposure at 400°C, isothermal ω particles precipitate at a greater rate in cold-rolled material than in the recovered, hot deformed state. SANS modelling is consistent with disc shaped nanoparticles, with length and radius under 6nm after thermal exposures up to 16 h. Modelling suggests that the nanoprecipitate volume fraction and extent of Nb partitioning to the β matrix is greater in the cold-rolled material than the extruded. The results show that nucleation and growth of the nanoprecipitates impart strengthening to the alloy.

Key words: Metals and Alloys, Precipitation, Transmission Electron Microscopy, TEM, Neutron Scattering, Titanium Alloys

1. Introduction

The use of β-titanium alloys in industry is steadily increasing due to their attractive properties. The low elastic modulus is of significance for orthopaedic applications, and the high yield strength is a requirement for aero applications such as landing gear. Ultimate tensile strengths far in excess of 1GPa have been reported [1, 2]. However, the mechanisms producing this level of strength are still not fully understood. Raghunathan *et al.* [3] attribute the high strength of Ti-10V-2Fe-3Al β-Ti alloy to fine scale α precipitates, which create a high number of β/α interfaces that hinder dislocation motion through the matrix. Nag *et al.* attribute high strength in a TNZT (Ti-Nb-Zr-Ta) β-Ti alloy to metastable B2 ordering in the matrix and found that precipitation of fine scale α particles destroyed this ordering, thereby softening the material [4].

The attribution of strengthening mechanisms in β-Ti alloys is further complicated by the metastable athermal ω (ω_{ath}) and isothermal ω (ω_{iso}) phases that can nucleate on quenching and appropriate ageing respectively. ω_{ath} forms from the *bcc* β lattice by displacement of two $\{111\}_\beta$ planes [5, 6]. It appears that the ω_{iso} phase is a continuation of the ω_{ath} transformation, such that after the ω_{ath} structure is formed, β stabilising elements are continuously rejected from the ω interface during isothermal ageing [7]. The precipitation mechanism from quenching to a stable precipitate on appropriate heat-treatment in a binary β-Ti alloy (Ti-18Mo wt.%) is believed to be $\beta \rightarrow \beta + \beta' \rightarrow \beta' + \omega \rightarrow \beta' + \omega + \alpha \rightarrow \beta' + \alpha$ [8], where β and β' are solute lean and solute rich *bcc* phases respectively. It is unknown if this precipitation path holds true for more highly alloyed β-Ti alloys.

Nag concluded that the dissolution of ω on ageing causes a reduction in hardness in Ti-15Mo [4], while Jones *et al.* concluded that the ω does not impart strengthening, and attributes an increase in strength to precipitation of nanoscale α laths in Ti-5Al-5Mo-5V-3Cr (Ti-5553) [9]. This brief literature review shows that there is much confusion over the strengthening phases in high strength β-Ti alloys. In this work, pinhole small angle neutron scattering (SANS) is used in conjunction with X-ray diffraction (XRD) and extensive complementary transmission electron microscopy (TEM) to study the precipitation process *in-situ* of Gum metal, a β-Ti alloy. The aim has been to implement an additional scientific technique to aid the un-

*Corresponding Author. Tel: +1 312 774 8634; fax: +1 847 467 2269

Email address: j.coakley06@imperial.ac.uk (James Coakley)

The term 'Gum metal' refers to an alloy composition range defined by Saito *et al.* that exhibit "super properties": ultralow elastic modulus, ultrahigh strength, superelasticity and superplasticity, at room temperature, as well as invar and elinvar properties [1, 10]. The fundamental composition of Gum metals are Ti-24(Nb+Ta+V)-(Zr,Hf)-O (at.%), and must satisfy specific values of average electron valence number, bond order and d-electron orbital energy, to ensure β phase stability. Thus a range of alloys may be referred to as Gum metal.

Table 1: Comparison of similar biomedical β-Ti compositions from the literature and that measured by Inductively Coupled Plasma Optical Emission Spectrometry (ICP-OES) and LECO analyses. All compositions are in weight % except for hydrogen (ppm).

Element, wt.%	Cr	Cu	Fe	H (ppm)	Hf	Nb	Ni	O	Ta	Ti	V	Zr
[1]	-	-	-	-	-	11.9	-	0.34	31	Bal	2.2	7.8
[1]	-	-	-	-	-	35.8	-	0.32	2.1	Bal	-	3.1
[19]	-	-	-	-	-	29.8	-	0.28	10.1	Bal	-	5.0
[19]	-	-	-	-	-	29.8	-	0.35	8.13	Bal	-	4.76
[15]	-	-	-	-	-	34	-	0.16	7	Bal	-	7
This work	<0.01	0.06	0.03	22	<0.05	36.2	<0.01	0.26	1.97	Bal	0.04	3.16

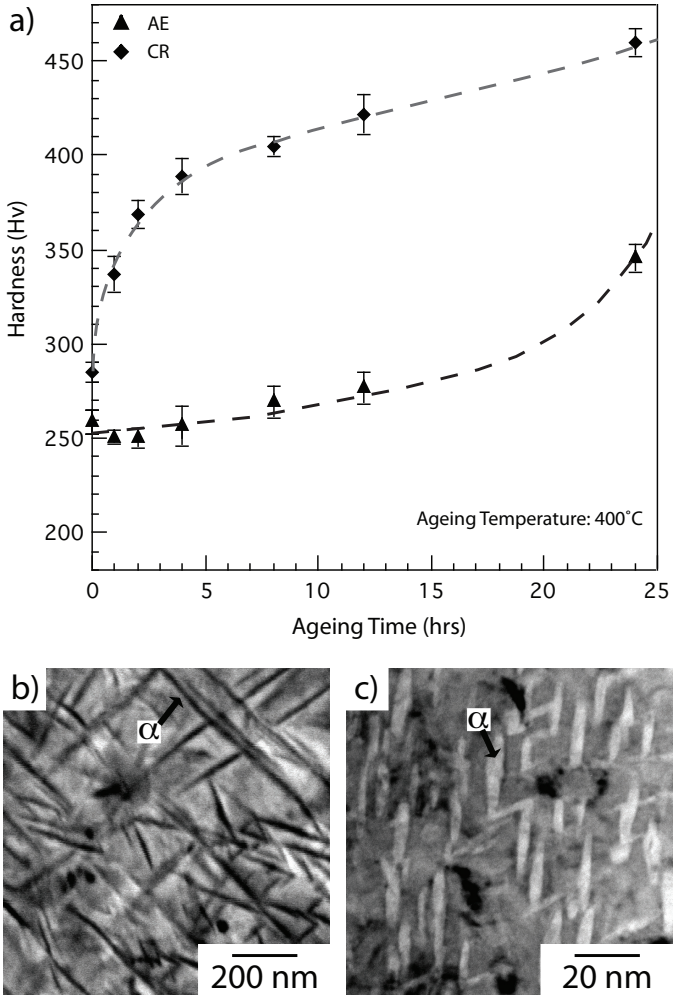

Figure 1: a) Evolution of micro-hardness of as-extruded (AE) and cold-rolled (CR) Gum metal, as a function of ageing time for heat-treatments between $1-24$ h at 400°C. Trendlines have been inserted to the data as a guide to the eye. b) Backscatter scanning electron microscope (BSEM) micrograph of the AE Gum metal microstructure following 24 h 400°C heat-treatment. c) The corresponding microstructure of the CR material with identical heat-treatment, imaged by bright field transmission electron microscopy (BF-TEM). Figures adapted from [17].

derstanding of precipitate strengthening in β-Ti alloys and shed light on contradicting theories published in literature.

The application of SANS to measure precipitation in engineering alloys *in-situ* (for example [11–14]) is infrequent and, to the authors' knowledge, has never been applied in the studies of Ti metallurgy. The bulk of SANS metallurgical research are *ex-situ* measurements. The experimental methodology employed in this work is similar to that of Collins *et al.* [11], who used *in-situ* SANS to study the coarsening kinetics in a nickel superalloy. To date, the experimental studies of precipitation in Ti metallurgy have been through TEM complemented by atom probe tomography and *in-situ* synchrotron X-ray diffraction (SXRD) [3, 9, 15, 16]. Each method has associated advantages and disadvantages. TEM remains the most important experimental method. However, these studies are *ex-situ* and frequently under conditions very different to the alloy's application conditions. SXRD can be employed to measure initial nucleation of phases *in-situ* by associating diffraction peaks to the appropriate phase [9]. SANS offers excellent insight into nano-scaled particle growth, but diffraction and scattering techniques require supporting TEM in order to be interpreted.

Two initial conditions of Gum metal were chosen to study precipitate nucleation and growth at 400°C by *in-situ* SANS: (i) as-extruded Gum metal; and (ii) as-extruded + 90% cold-rolled Gum metal. These initial conditions were selected based on a study of the evolution of micro-hardness with ageing time and temperature, Figure 1a. It is observed that cold-rolling increases the hardness, as expected. The evolution of hardness with different ageing times at 400°C is significantly different in the cold-rolled material than the as-extruded. This phenomenon is due to very different precipitation behaviour in the two materials [17]. The microstructures following a 400°C 24 h heat-treatment of both Gum metal conditions are presented in Figures 1b and c. BF-TEM and BSEM techniques cannot resolve the ω phase. The α particles observed are an order of magnitude smaller in the CR condition, and an investigation of the precipitation mechanisms is warranted.

2. Experimental Details

The Gum metal studied was produced by ingot metallurgy from compacted pure elements. The furnace was back-filled with high purity argon and the elements melted by a He plasma torch. Following cooling and solidification, the ingot was inverted and remelted. This inversion and remelting process was performed three times to improve homogeneity. A 60 mm diameter billet was machined from the button and solution treated at 850°C for 60min. The

billet was coated in Deltaglaze TM 3418 (Acheson, MI, USA) glass lubricant. The billet was then heat-treated at 975°C for 105 min prior to extrusion to 12 mm diameter rod. A section of this extruded rod was then cold-rolled to 90% strain. In this work, the as-extruded Gum metal is labelled AE, and the as-extruded + 90% cold-rolled is labelled CR, for convenience.

Pole figures previously published for 90% strain cold-rolled Gum metal suggest that a $\{001\}<1\bar{1}0>$ texture is formed. This is in agreement with *bcc* rolling textures in other materials [18].

The composition of the extruded bar was verified by inductively coupled plasma optical emission spectrometry (ICP-OES) and LECO analyses for the oxygen and hydrogen content. This is presented in Table 1, along with a selection of similar biomedical β-Ti alloys published in literature. The alloy produced for this work was based on Saito's original publication and is in good agreement [1].

2.1. Microscopy

Specimens for optical microscopy were prepared by mechanical polishing and etched using 8 vol.% HF and 15 vol.% HNO_3 in water. The initial average grain size was measured by analysis of the optical micrographs using the ImageJ software analysis package.

Specimens for TEM were removed by spark-erosion and thinned using twin-jet electropolishing in a solution of 8 vol.% H_2SO_4 in methanol at −40°C and 18 V. TEM foils were examined using a JEOL TEM 2000FX microscope and a FEI TITAN 80/300 TEM/STEM (Scanning Transmission Electron Microscopy).

The heat-treatment times studied in TEM were selected based on the SANS results, shown in Figure 8. The microstructures following 0.25 h, 2.5 h, 12.5 h and 16 h 400°C thermal exposures resulted in very different SANS scattering curves, warranting TEM studies, along with the two initial sample conditions. These heat-treatments were repeated in order to produce samples for microscopy, and all microscopy was performed *ex-situ* at room temperature following air cooling of the samples.

2.2. X-ray Diffraction

Laboratory XRD measurements were performed on the AE and CR SANS samples following the SANS experimentation. XRD was performed on a PANalytical X'Pert Pro MPD fitted with an X'celerator detector, using Cu-K_α X-ray radiation with a characteristic wavelength of 1.541Å at 40kV and 40mA current. Data were collected over a range of 20 - 100° 2θ for 1 hour. Phase identification was performed using CrystalDiffract software with crystal structure parameters of pure Ti α [29], β [30], ω [31], and α'' [18] phases.

2.3. Small Angle Neutron Scattering

SANS measures the shape and intensity of the coherent elastic scattering at small angles from the incident beam,

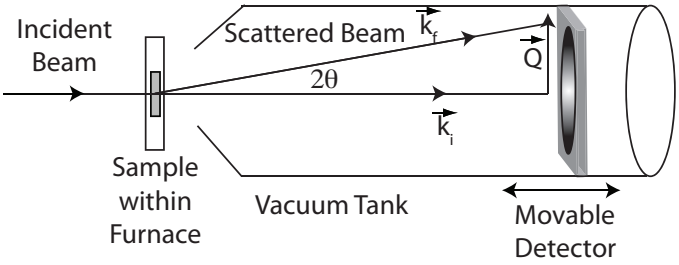

Figure 2: Schematic of the experimental arrangement used to perform small angle neutron scattering at HFIR, ORNL, Tennessee, USA.

with angles far smaller than classical diffraction angles [20–27], typically under 5°. Thus pinhole SANS (Figure 2) can provide diffraction patterns from structures or fluctuations in composition or density on distance scales of about 1 to 100 nm, commensurate with the size of smaller precipitates in metal alloys.

In this work, SANS was performed at Oak Ridge National Laboratory (ORNL) High Flux Isotope Reactor (HFIR) General Purpose Small Angle Neutron Scattering (GP-SANS) instrument [28]. The set-up is illustrated in Figure 2. A mechanical velocity selector defines the incident neutron wavelength $\lambda = 4.75$ Å with a 10% spread, and the beam is collimated prior to the sample by a pair of apertures. $\mathbf{k_i}$ is the incident wave vector with magnitude $k = 2\pi/\lambda$. The scattering vector $\mathbf{Q}$ is the difference between incident and scattered wave vectors $\mathbf{Q} = \mathbf{k_f} - \mathbf{k_i}$. The magnitude of Q quantifies the lengths of the reciprocal space $Q = \frac{4\pi}{\lambda}\sin\theta$, where 2θ is the scattering angle.

10 mm × 10 mm square samples of the AE and CR Gum metal were ground to a thickness of 1 mm for experimentation, finishing with 1200 grit paper. Two SANS experiments were performed, the first on a CR sample, and the second on an AE sample under identical test conditions.

A SANS-specific argon gas atmosphere furnace was placed in the beam-line. The sample to detector distance was set at 6 m, an aperture of 6 mm was used, and measurement count times were 900 s. The 1 m square 8 mm diameter linear gas tube helium detector array was offset from the centre in the y-axis in order to measure a larger Q range.

The SANS raw data was reduced to absolute scattering probabilities $\partial\Sigma(Q)/\partial\Omega$ using standard software in the HFIR Wavemetrics Igor package [28]. Data were corrected for: transmissions $T(\lambda)$ measured with the central beam stop removed and the incident beam attenuated, for backgrounds from the empty furnace, for dark current background in the detector, and with the isotropic scattering from a 3 cm thick Plexiglas plate for detector pixel sensitivity variations. Data were placed on the absolute scale by the ratio of the area detector count rate to the beam-monitor count rate in the empty-beam transmission measurement for each wavelength.

After collecting room temperature data on each alloy

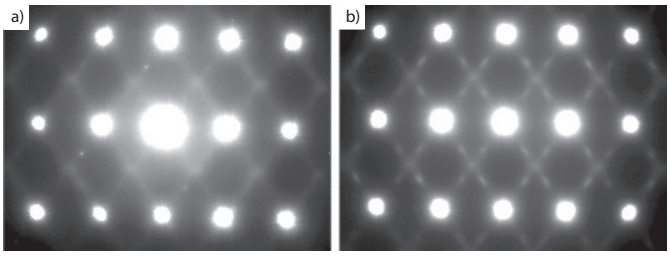

Figure 3: Gum metal TEM diffraction patterns of $<110>_\beta$ zone axis in the a) as-extruded (AE) and b) 90% cold-rolled (CR) conditions.

sample, the furnace temperature was raised to 400°C at ∼ 1°C/s, and the elevated temperature *in-situ* measurements were recorded every 15 minutes for 12.5–16h.

3. Results

3.1. Microscopy

Figure 3 shows two electron diffraction patterns from TEM for the two sample initial conditions viewed parallel to the $<110>_\beta$ zone axis. The AE pattern (Figure 3a) shows streaking along the $\{112\}_\beta$ which is associated with ω_{ath} [15, 16]. The intensity due to ω_{ath} was greater in the CR diffraction pattern (Figure 3b). It is reasonable to assume that the microstructure at room temperature is representative of the microstructure at 400 °C, as it is well below the beta transus temperature (typically 600 °C – 800 °C for metastable β-Ti alloys).

The evolution of the TEM diffraction patterns with ageing times at 400°C is presented in Figure 4, for both the AE and CR conditions. The longest ageing times (AE: 12.5 h, CR: 16 h) represent the AE and CR microstructures at the end of the SANS experiments. A key diagram is provided in Figure 4g for ω and 4i for α. After 0.25 h ageing time, the AE sample exhibits faint streaking in the $\{112\}_\beta$. Spots are seen forming after 2.5 h at 1/3 and 2/3 $\{112\}_\beta$, growing in intensity after 12.5 h and forming more distinct spots. There are no clear spots from α in the diffraction pattern following the AE 12.5 h heat-treatment, however there is a very weak suggestion this phase may be present in the 2.5 h pattern. TEM imaging confirmed the nanoprecipitation is predominantly ω during heat-treatment of the extruded material, and extensive ω precipitation is evident in Figure 5e. The very faint spots in some of the TEM diffraction patterns at 1/2 $\{112\}_\beta$ are associated with the α'' martensitic phase, according to the schematic of Talling *et al.* [18]. The reflections are too weak to image this phase. Furthermore, previous imaging of this phase in deformed Gum metal has shown they are of a size greater than that measured in SANS in this work [18].

The CR material shows much less streaking in the $\{112\}_\beta$ at all time scales compared to the as-extruded material. There are distinct diffraction spots observed at 1/3 and 2/3 $\{112\}_\beta$ after 0.25 h heat-treatment, that grow in intensity and become more distinct with prolonged thermal exposure. There is some evidence of α diffraction spots in the 2.5 h diffraction pattern (Figure 4d), and definite α diffraction spots in Figure 4h following 16 h heat-treatment.

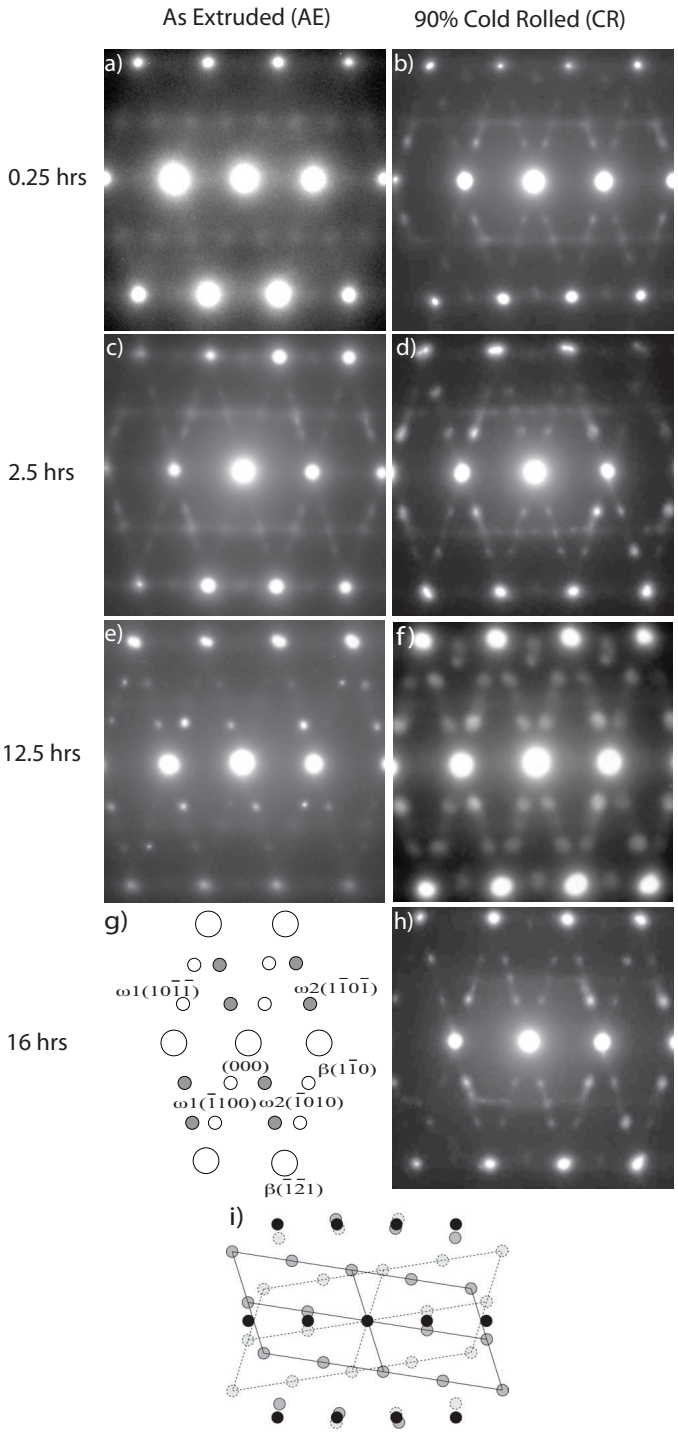

Figure 4: TEM diffraction pattern evolution for ageing times of 0.25 h – 16 h at 400°C of AE and CR Gum metal. The diffraction patterns are of the $<113>_\beta$ zone axis and the reciprocal lattice streaking and spots observed at 1/3 and 2/3 $\{112\}_\beta$ are due to the ω phase. j) Schematic. Black: β spots; grey: α spots

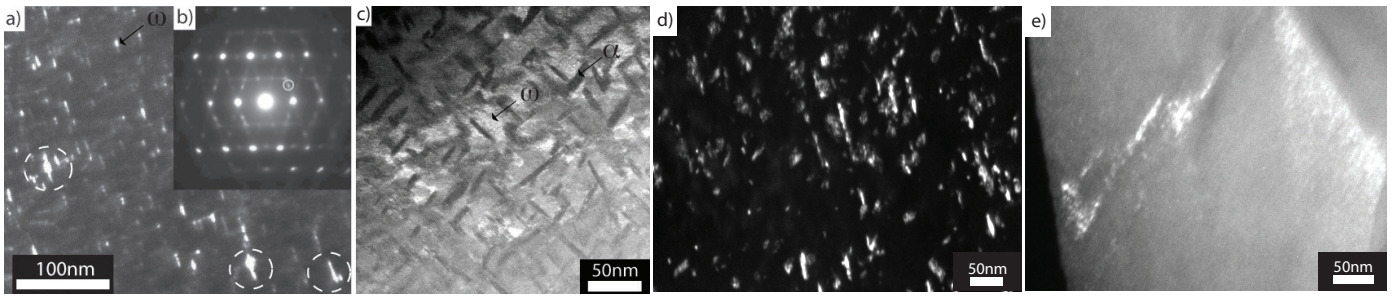

Figure 5: a) Dark-field image of cold-rolled Gum metal after 0.25 h ageing at 400°C. Regions where α may be precipitating from ω are highlighted. b) TEM diffraction pattern on the $<113>_\beta$ zone axis for the same material as (a). The spot used to take the dark-field image (a) is highlighted. c) ADF STEM image of cold-rolled Gum metal with a 16 h 400°C heat-treatment. d & e) Dark field TEM from the same ω reflection as Figure 5b of cold-rolled Gum metal with a 16 h 400°C heat-treatment and extruded Gum metal with a 400 °C 12.5 h heat-treatment respectively.

It was possible to obtain dark-field TEM images of the ω particles based on the ω diffraction spots for all AE samples with heat-treatment times at and above 2.5 h, and CR samples of times at and above 0.25 h. A dark-field image for CR material + 0.25 h 400°C heat-treatment is given in Figure 5a, with the 1/3 $\{112\}_\beta$ diffraction spot used to obtain the micrograph highlighted in Figure 5b. It is interesting to note that rods or plates may grow from the circular ω particles, highlighted in Figure 5a. Both the α and ω phases may be observed if their associated reflections slightly overlap, so the rods may be α particles. The circular ω particles range in size from approximately $3 - 20$ nm after the longest heat-treatment of 16 h in the CR material, Figure 5d. A number of rod shaped particles are also observed.

ADF STEM-imaging of CR material after 16 h ageing time shows α particles of approximately 50 nm length, along with what appears to be a substantial amount of very fine particles $\sim$ 10 nm in diameter, believed to be ω_{iso}, Figure 5c. Energy Dispersive X-ray (EDX) analysis of the larger precipitates showed a lowered Nb content, which is expected of the α. Comparing the STEM image of Figure 5c to the dark field image of Figure 5d from a 1/3 $\{112\}_\beta$ ω diffraction spot, it is clear that extensive ω particles are in the channels between the α precipitates, following 16 h 400°C heat-treatment of the CR material.

3.2. X-ray Diffraction

XRD measurements of the CR and AE samples following SANS experimentation are presented in Figure 6a and b respectively. The CR measurement shows strong single $(001)_\omega$ and $(002)_\omega$ peaks. The broad high intensity peak at 61 ° in the CR data appears to be a compound peak of the $(120)_\omega$ and the $(110)_\alpha$, with a single $(010)_\alpha$ peak at 31 °. Care must be taken of the peaks observed at 50 ° in the CR diffraction pattern, and at 35 ° in the AE pattern. These peaks may arise from Cu K_β which hasn't been completely removed with the secondary monochromator.

There is a single $(001)_\omega$ peak in the AE diffraction pattern. $(010)_\alpha$ is labelled, however it is very dubious due to the peak location also lying on a α'' peak position and the Cu K_β $(011)_\beta$ position. The $(022)_\beta$ is a doublet due to $K_{\alpha 1}$ and $K_{\alpha 2}$.

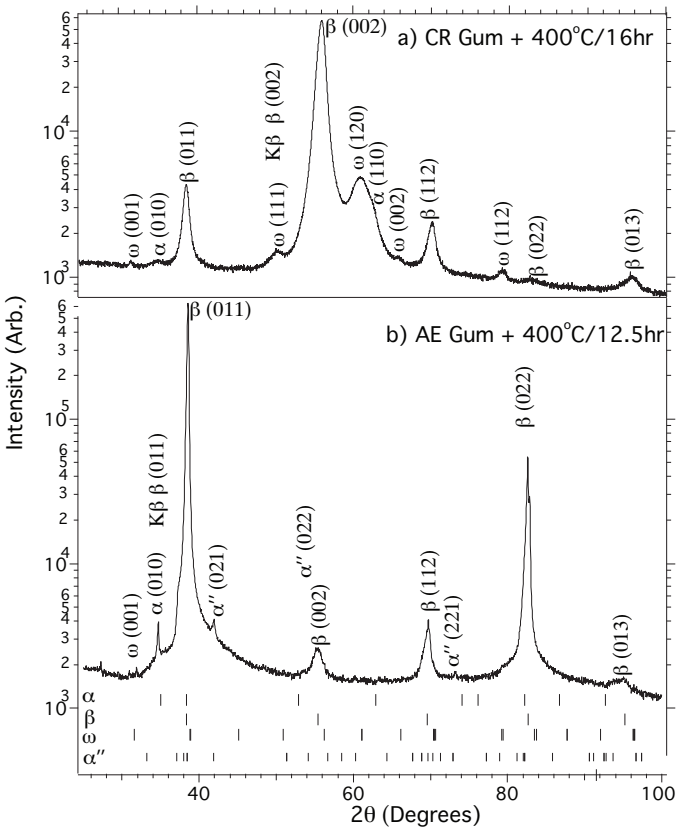

Figure 6: XRD of the CR and AE SANS specimens following heat-treatments of (i) 400 °C/16 h and (ii) 12.5 h respectively.

3.3. Small Angle Neutron Scattering

Examination of the raw SANS data showed that the AE material scattered neutrons isotropically, while the scattering from the CR material has some modest anisotropy, Figures 7 (a) and (b) respectively. The vertical lines seen in Figure 7a and b are from the different vertical detector tubes. Cold-rolling the material produces crystallographic texture in the sample [32]. Thus, the anisotropy

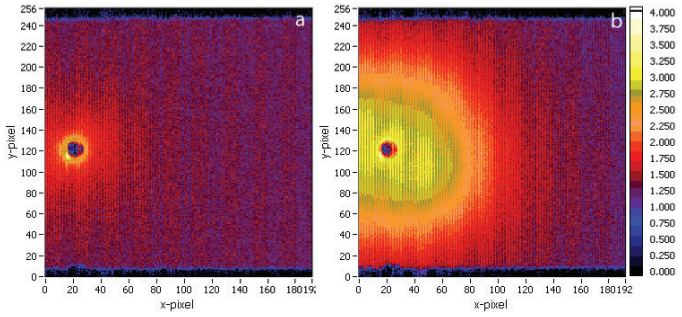

Figure 7: Raw SANS data from gas tube detector array after 7.5 h at 400°C: (a) as-extruded material, (b) cold-rolled sample.

is believed to be a consequence of particle orientation arising from texture formation due to the cold-rolling process. The thickness of the sample when mounted in the beam was normal to the rolling direction. Although in principle the anisotropy in the SANS pattern provides further information, the data was azimuthally averaged for both samples. The analysis of anisotropic patterns would add extra fitting parameters and for the disc shaped particles proposed, would require extensive numerical simulations, which would not be justified by the limited amount of extra information that might be acquired.

Selected scattering curve evolution with time and model fits are presented for both the AE and CR samples, Figure 8. The error bars have been removed as they obscure the data, but on average are $\sim \pm 0.01\,\mathrm{cm}^{-1}$.

The scattering curve evolution of the AE sample is markedly different to that of the CR sample, both in shape and evolution rate. The scattering curve evolution of the AE sample is slow when compared to the CR material, with very little change at $Q < 0.01\text{Å}^{-1}$, and $Q > 0.01\text{Å}^{-1}$. A broad scattering profile is seen to develop in the AE data, and is very apparent after 12.5 h, between $0.01\text{Å}^{-1} < Q < 0.06\text{Å}^{-1}$.

The CR scattering curve evolves far more rapidly across the whole of the Q range measured. The intensity at low Q is much greater than those seen in the AE test. There is a clear scattering peak after 0.25 h, *i.e.* the first measurement taken at 400 °C. This peak grows in magnitude and shifts to lower Q up to 6.25 h. Such peaks or maxima in SANS most often imply closely packed smaller particles, thus providing information on both particle size and interactions or spacings as discussed below. A plateau region is seen in the measurements after this time, shown for 12.5 h and 16 h, with very slow scattering curve evolution occurring at these later times compared to earlier ones in the test.

4. Discussion

4.1. Transmission Electron Microscopy

The streaking along the 1/3 and 2/3 $\{112\}_\beta$ observed in both initial conditions (Figure 3) is associated with ω_{ath}

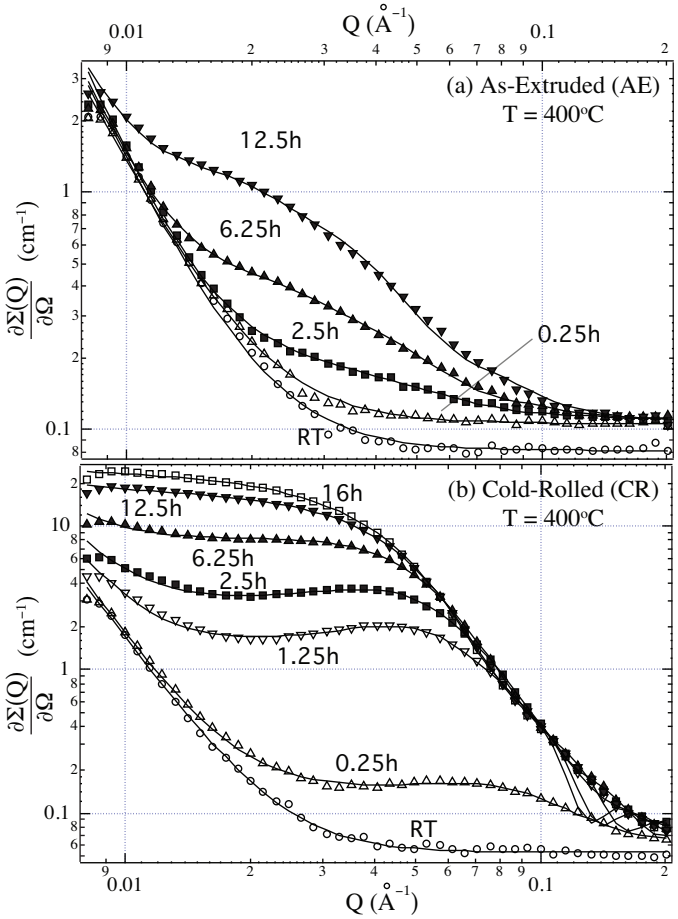

Figure 8: The evolution of SANS scattering curves with time measured *in-situ* at 400°C for (a) as-extruded Gum metal (AE), and (b) as-extruded + cold-rolled Gum metal (CR), plotted on a log-log scale. The times represent the time at which the measurement was finished, with each measurement taking 0.25 h. Solid lines are fits to the data which include monodisperse discs. Poor fits at high Q for $t \geq 6.25$ h in the CR condition can be improved with a polydisperse disc model.

within the β [15, 16]. The greater intensity in the CR material suggests that ω_{ath} is enhanced as a consequence of plasticity. During thermal exposure at 400°C, the streaking is seen to shift to distinct spots at 1/3 and 2/3 $\{112\}_\beta$ in both materials (Figure 4), due to completion of the $\{111\}_\beta$ plane collapse. This ω phase is termed ω_{iso}, and is due to diffusion induced chemical rearrangement of atomic species. The kinetics appear to be much more rapid in the CR material than the AE material. The reason for this may be two fold: (i) there is greater ω_{ath} initially present in the CR material; (ii) the CR material possesses a greater dislocation density. These may act as further ω nucleation sites, and also act as fast diffusion paths.

α particles appear to grow from the ω_{iso} phase, seen in the dark-field TEM micrograph in Figure 5a. This has been observed previously in Gum metal [15], and in Ti-5553 [16]. However, this conclusion must be treated with caution, as the two precipitates do not necessarily lie in the same plane, and could simply be above one another within

the thickness of the foil. Also, as mentioned previously, it is not possible to define a phase based on precipitate shape alone.

The TEM diffraction patterns and the dark-field imaging give strength to the suggestion that precipitation occurs in the following order: $\beta \rightarrow \beta + \omega_{\text{ath}} \rightarrow \beta + \omega_{\text{iso}} \rightarrow \beta + \alpha$, when heat-treated above the β solvus, quenched, and subsequently aged at 400°C. β in this case refers to the *bcc* phase in general, as we have no specific evidence in the present case to support the decomposition of the β.

It is notable when performing the TEM that both ω_{ath} and ω_{iso} nucleation were far more localised in the AE material than the CR material, evident on comparison of Figures 5e and 5d respectively. The CR ω was generally quite evenly distributed through the grains in all heat-treatment conditions. This is not true for the AE material, where the ω particles were present in localised regions of certain grains in all heat-treatment conditions, Figure 5e. The diffraction patterns presented in Figure 4 were selected as they illustrate the ω evolution, however it is possible to image areas with very little ω reflections in the AE material. If the ω particles provide precipitate strengthening it is desirable that they are evenly distributed through the grain, as is the case for the CR material.

It was observed that when comparing STEM to dark-field TEM that the area fractions of the precipitates are markedly different. It is impossible to make estimates or comparisons of ω volume fraction based on dark-field TEM imaging for a number of reasons, namely: (i) the image is based on just one lattice reflection; (ii) the thickness of the sample will contribute to the area fraction of particles observed; and (iii) the image area is an area of one grain and may not be representative of the bulk material. The inability to compare the extent of nano-precipitation by TEM methods is reason to attempt *in-situ* SANS measurements of the precipitation process. The TEM studies described are used as a guide to the modelling and interpretation of the SANS data.

4.2. X-ray Diffraction

The ω phase is not easily detected by laboratory XRD. The clear peaks from the CR material after 16 h thermal exposure are evidence of extensive ω precipitation. The strong peak at $(002)_\beta$ arises from the cold-rolling process. The AE material produces much weaker diffraction from the particles and are difficult to identify from background, implying that the nanoparticles have a much lower volume fraction compared to the CR material.

4.3. Small Angle Neutron Scattering Modelling

A number of software programs exist to facilitate least squares fits to SANS data, notably the NIST SANS package used with Wavemetrics Igor Pro [33], FISH developed at ISIS [34] (used in this work), and SASVIEW [35].

The probability of small angle neutron scattering from uniform monodisperse particles is

$$\frac{\partial \Sigma(Q)}{\partial \Omega} = NV^2(\Delta\rho)^2 P(Q)S(Q) + \text{BKG} \qquad (1)$$

where N is the number of particles per unit volume, V is the volume of one particle, and $P(Q)$ is the particle form factor or shape function. Note that the dispersed particle volume fraction $\phi = NV$. $P(Q)$ depends on the size and shape of the particle and is normalised such that $P(Q = 0) = 1.0$ [36]. $S(Q)$ is the interparticle structure factor, which tends to 1.0 for sufficiently dilute systems, but otherwise allows for interparticle interactions. BKG is any residual background not allowed for in the data reduction, often a flat term for incoherent scattering from certain elements, such as hydrogen. $\Delta\rho = \rho_{\text{ppt}} - \rho_{\text{matrix}}$ is the neutron scattering length density difference between the particle and its matrix. The scattering length density of phase x is

$$\rho_x = (\rho_{\text{mass}} N_A / M_r) \Sigma n_i b_i \qquad (2)$$

where ρ_{mass} is the phase mass density, N_A is Avogadro's number, M_r is the molecular weight of the phase, n_i is the atomic fraction of element i in the phase, and b_i is that element's associated neutron scattering length. A few isotopic species, including H and Ti, have negative scattering lengths. Unlike X-rays where scattering is proportional to atomic number, neutron scattering lengths vary erratically across the periodic table, so it is not immediately apparent which phases have strong neutron scattering contrast relative to the matrix in the alloy studied here.

The general form of $P(Q)$ is given by van de Hulst's equation [37]

$$P(Q) = \frac{1}{V^2} \left| \int_0^V \exp[if(Q\alpha)] dV \right| \qquad (3)$$

where α is a "shape parameter". Analytical expressions exist for most common shapes and more complex shapes can be deduced from these. Taking the case of rod (or disc) shaped particles of length L and radius R, the form factor is given by

$$P(Q) = \int_0^{\pi/2} F^2(Q) \sin(\gamma) d\gamma \qquad (4)$$

where

$$F(Q) = \frac{\sin(\frac{1}{2} QL \cos\gamma)}{\frac{1}{2} QL \cos\gamma} \frac{2J_1(QR \sin\gamma)}{QR \sin\gamma} \qquad (5)$$

in which $J_1(x)$ is the first order Bessel function, and the equation requires numerical integration over angle γ between the Q vector and the angle of the rod [34, 38].

At higher volume fractions, interference from waves scattered by adjacent particles occurs, and is accounted for by the interparticle structure factor S(Q). The simplest

structure factor is for impenetrable hard spheres, for which the Percus-Yevick approximation was solved analytically by Ashcroft and Lekner [39]. As the hard sphere volume fraction increases S(Q) pushes down the SANS intensity at small Q, eventually giving a peak at approximately 2π divided by the mean particle separation. S(Q) always tends to 1.0 at high Q.

Ashcroft and Lekner derived S(Q) = 1/(1-C(Q)) where $C(Q)$ is an expression containing the volume fraction (V_{HS}) and diameter (D) of the hard spheres.

$$\begin{aligned} C(Q) = &-\frac{24V_{HS}}{(QD)^6}\{\alpha(QD)^3(\sin QD - QD\cos QD) \\ &+ \beta(QD)^2[2QD\sin QD - (Q^2D^2-2)\cos QD \\ &- 2] + \gamma[(4Q^3D^3 - 24QD)\sin QD - (Q^4D^4 \\ &- 12Q^2D^2 + 24)\cos QD + 24]\} \end{aligned} \tag{6}$$

and $\alpha = (1+2V_{HS})^2/(1-V_{HS})^4$, $\beta = -6V_{HS}(1+\frac{V_{HS}}{2})^2/(1-V_{HS})^4$, $\gamma = \frac{1}{2}V_{HS}(1+2V_{HS})^2/(1-V_{HS})^4$.

In order to deduce microstructural parameters from the reduced SANS scattering curves (Figure 8), FISH [34] was employed to produce a model that fits to the data. Various combinations of particle shapes were used, based upon TEM, and a successful model combination was found. Discussing the model in its constituent parts:

a) Background BKG. A small flat background was included to account for incoherent scattering, which varies a little with temperature.

b) Porod Scattering aQ^{-4}. The Porod limit [40] shows that for a smooth particle with sharp interfaces the intensity decreases proportional to Q^{-4} at high Q

$$I(Q)_{Q\to\infty} = 2\pi S(\Delta\rho)^2 Q^{-4} \tag{7}$$

where S is the surface area per unit volume. The power term was initially left as a fitting parameter, as values towards -3 indicate rough or fractal interfaces, but here it always tended towards -4, so was left fixed, reducing the number of fitting variables. $a = 2\pi S(\Delta\rho)^2$ is a fitting parameter in the model. Large micron sized grains were observed in the as-extruded material by optical microscopy, thus the Porod scattering potentially arose from the interfaces of these larger particles, which would create a scattering peak at a lower Q than that resolvable in this measurement.

c) P(Q) Discs. From TEM (Figure 5), the scattering observed could be due to the ω phase, α phase, or both, depending on the processing condition and thermal exposure times. These have circular or rectangular 2-dimensional shape respectively when viewed in TEM. There is a variety of three dimensional shapes that correspond to the 2-D projections observed in micrographs. For example, the observed ω circle may correspond to a disc, sphere, lenitcular-shape [15] etc. A model of randomly oriented discs gave best agreement with the SANS data. Though this may not be a unique interpretation, it is supported by the TEM images. A schematic defining the disc radius (R) and length (L) is inset in Figure 10a.

d) S(Q) Hard Spheres (HS). As previously discussed, with higher volume fractions, scattering due to interparticle interference arises. This is accounted for using the hard sphere interparticle structure factor that multiplies the form factor for randomly oriented discs. The HS model is only an approximation for non-spherical particles in a metal alloy, but it is a reasonable one for modest aspect ratio particles at modest volume fractions, without interpreting the fitted values of the hard sphere radius and hard sphere volume fraction too literally. At very high volume fractions preferred orientations of anisotropic particles become important, requiring complex numerical simulations.

The full model is therefore described by

$$\partial\Sigma(Q)/\partial\Omega = P(Q)_{\text{Discs}}S(Q)_{\text{HS}} + aQ^{-4} + \text{BKG} \tag{8}$$

where $P(Q)_{\text{Discs}}$ is given by Equation 4 and $S(Q)_{\text{HS}}$ by Ashcroft and Lekner [39], discussed previously. $P(Q)_{\text{Discs}}$ has three fitting parameters: scale (a fitting parameter particular to FISH equal to $10^{-24}\phi(\Delta\rho)^2$), disc radius R, and disc length L. If the scattering contrast $(\Delta\rho)^2$ is known, the volume fraction ϕ can be determined from the scale factor or vice-versa. $S(Q)_{\text{HS}}$ has two fitting parameters, the hard sphere radius R_{HS} and the hard sphere volume fraction V_{HS}. Though this may be an effective approximation for non-spherical particles, the hard sphere volume fraction should be similar to that from $P(Q)_{\text{Discs}}$ in a good fit. The final fitting parameter is a of the Porod scattering. Thus, the model is composed of just 6 fitting parameters in total, all of which have physical meaning. Initial estimates of these parameters are introduced into the model, and the model fit converges to the least squares minimum with the data by the Marquadt method.

An example of the full model fit to a SANS measurement of the cold-rolled sample after t = 1.25h at T = 400°C is shown in Figure 9. This figure also shows the contribution of each component of the model. The fits show good agreement for the RT measurements of both the AE sample and CR sample, and can be fitted with just Porod scattering + BKG. This is illustrated on comparing the shape of the curve aQ^{-4} + BKG in Figure 9 to the RT scattering curve (Figure 8a and b). There is perhaps a suggestion of a very small peak at $Q \sim 0.035\text{Å}^{-1}$ in both room temperature measurements (Figure 8a and b), but it was decided not to over fit the data. From the electron diffraction patterns, there are evidently fine ω particles present in both initial conditions, seen as streaking along the $\{112\}_\beta$ in Figure 3a and b. ω_{ath} has the same composition as the β matrix [7] and thus has no neutron scattering contrast. This explains why no scattering peak is observed initially, even though ω particles are clearly present in the TEM diffraction patterns.

A scattering peak forms immediately in the cold-rolled sample during thermal exposure at 400°C (Figure 8b), but not in the as-extruded sample (Figure 8a), which can still

be fitted with a Porod + BKG curve shape at $t = 0.25$ h. Following this, it is not possible to accurately fit the data without the form factor $P(Q)$. The scattering peaks that form in both SANS experiments are due to the formation of a phase with a different composition to the matrix. The as-extruded data did not require a structure factor term to fit the data, indicating a lower volume fraction.

The model fits were not as good at high Q at later time scales, in both experiments. The slight fitting error that occurs can be corrected by accounting for polydispersity in the model (effectively smoothing the peak shape at high Q). The form factor used in FISH is for a monodisperse system. SASVIEW was used to confirm that polydispersity improves the model fit, and there was good agreement of mean particle size between the models.

The model fit results illustrating the evolution of disc radius, length, and $\phi(\Delta\rho)^2$ during thermal exposure are shown in Figures 10a - c. The physical shapes of the discs are different in the CR and AE samples, Figure 10a. From $1 \rightarrow 16$ h the CR has a length to diameter ratio $L/2R \sim 0.45$, while the ratio for the AE sample between $3.5 \rightarrow 12.5$ h is $L/2R \sim 0.2$. The growth of the average particle size appears to be quite similar, between $1-12.5$ h the particle radius increases by 2 nm and length by 1.5 nm, while the AE average radius increases by 1.6 nm and the length increases by 2 nm, respectively. It is important to reiterate that these values are based on the assumption that scattering is arising from a single size distribution of disc-shaped precipitates. It is justifiable to state these disc-shaped dimensions producing scattering correspond to the ω phase for the extruded data based on TEM, however the cold-rolled sample also nucleates extensive α so

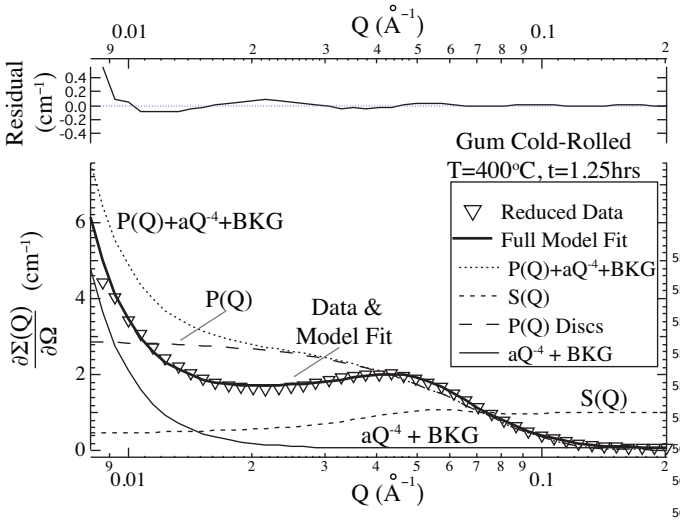

Figure 9: An example of the SANS model fit used in this work for the cold-rolled Gum metal at $t = 1.25$h during thermal exposure at $T = 400°$C. Q is plotted on a log axis. The graph illustrates the components of this model, where the overall model fit is defined as $P(Q)S(Q) + aQ^{-4} + \text{BKG}$. The scattering from S(Q) is further illustrated by comparing the full model fit to the fit of $P(Q)+aQ^{-4}+$ BKG *i.e.* by comparing to a fit with no scattering factor.

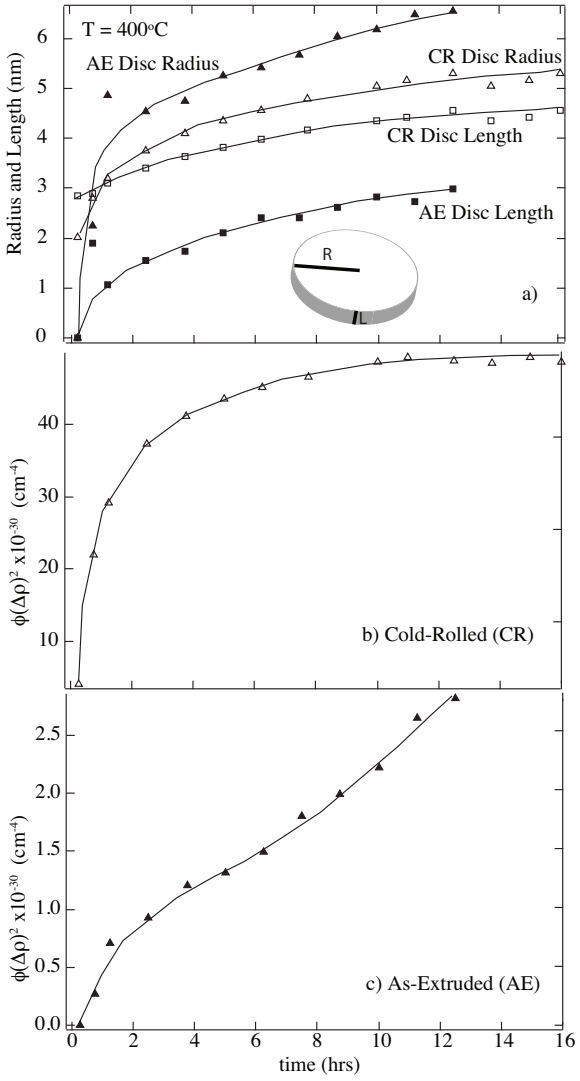

Figure 10: SANS model fit results for *in-situ* measurements during 400°C thermal exposure on an as-extruded (AE) and cold-rolled (CR) sample. a) Disc radius and length of both processing conditions. b and c) Cold-rolled and as-extruded $\phi(\Delta\rho)^2$ term respectively. The curves through the data points are guide for the eye fits. Inset a) Schematic defining the disc radius (R) and length (L).

the SANS model may be too simple to represent the cold-rolled data. As a unimodal model fits the data well, it would likely be fruitless to pursue a multimodal model that wouldn't simply be overfitting to the data.

Subtracting the hard-sphere diameter from either the particle diameter or length should give an approximation to an interparticle distance of the system. The interparticle distances are $\lambda_d \sim 8$ nm for CR + 6.25 h heat-treatment (where the structure factor is apparent), and $\lambda_d \sim 20$ nm for AE + 6.25 h heat-treatment. These values seem reasonable, but again care must be taken when interpreting the cold-rolled material data.

The SANS data shows that the magnitude and evolution of the term $\phi(\Delta\rho)^2$ are dramatically different between the CR and AE cases, Figure 10b and c. It is evident that

particle evolution and growth during thermal exposure is far more rapid in the CR material than the AE material. As previously discussed this is most likely due to the CR material possessing a higher initial number density of ω_{ath} and a greater dislocation density.

From Equation 5, it is clear that the volume fraction ϕ can only be deduced from the SANS model if the scattering length density contrast $\Delta\rho$ is known. A Fortran model was developed which took the $\phi(\Delta\rho)^2$ term as input for each thermal exposure. The initial model used the average phase compositions from an atom-probe composition profile published by Nag *et al.* in a very similar alloy as input [15]. The scattering length of each element in the alloy is $b_{\text{Ti}} = -3.4382 \times 10^{-5}$Å, $b_{\text{Nb}} = 7.0543 \times 10^{-5}$Å, $b_{\text{Zr}} = 7.1630 \times 10^{-5}$Å, and $b_{\text{Ta}} = 6.91703 \times 10^{-5}$Å [41]. Each phase's mass density ρ_{mass} and molecular weight M_r were calculated from first principles, based on the atomic weights and densities of each element in each phase and the atomic fraction in each phase from Nag [15], and thus the scattering length densities of each phase ρ_x were calculated from Equation 2. This allowed for volume fractions to be outputted, Equation 5. The model incorporated a check for conservation of matter (i.e. the lever rule). According to Nag *et al.* the α phase is initially depleted in Ti [15], and the scattering length densities calculated from this work are $\rho_\beta = -0.27 \times 10^{10}\text{cm}^{-2}$, $\rho_\alpha = 0.24 \times 10^{10}\text{cm}^{-2}$, $\rho_\omega = -0.73 \times 10^{10}\text{cm}^{-2}$. Based on this work the absolute values of the scattering length density contrast of each phase with the matrix are very similar: $|\rho_{\omega-\beta}| = 0.46 \times 10^{-10}\text{cm}^2$ and $|\rho_{\alpha-\beta}| = 0.51 \times 10^{10}\text{cm}^{-2}$.

Applying this methodology to the monodisperse disc model gives a reasonable volume fraction ϕ for the AE data (13% after 12 h heat treatment) for the ω phase, however the CR data reaches 240% after 16 h heat treatment. The sensitivity of the model to Ti and Nb distributions between phases was checked, and shown to be extremely sensitive. Altering the Ti and Nb in each phase by 5 at.% (*i.e.* further depleting the ω_{iso} phase of Nb) from the values published by Nag *et al.* [15] decreases the predicted volume fraction by an order of magnitude.

From the earlier discussion of the TEM diffraction patterns it is justifiable that scattering arises due to the ω phase alone in the AE material. The CR analysis cannot be so conclusive due to α spots also present in the final TEM diffraction pattern. The XRD provides evidence that extensive amounts of ω and α are present in the CR material after 16 h heat treatment. Various SANS models were tried for the cold-rolled data based on the 2D micrographs that might better represent the microstructures, including platelets and rods with initial inputs of $L = 50$nm to check for convergence, however a satisfactory model was not found. The fact that disc shaped particles fit the cold-rolled data so well is not conclusive evidence that the scattering observed is arising from the ω phase alone. The α particles have similar width to the SANS model output diameters. Due to a number of reasons including i) scattering anisotropy arising from particle orientation, ii) possibly similar scattering length density contrasts of the two phases of interest, iii) and that a simple unimodal model fits the data so well, it may not be possible to produce a satisfactory SANS model for the complicated case of co-precipitation of ω and α in the cold-rolled material.

As Nb, Zr, and Ta all have similar scattering lengths, and the atomic fraction of Zr and Ta are low in this alloy (2 at.% and 1 at.% respectively), it is possible to treat the alloy as a binary Ti-Nb system for the SANS data analysis. The Fortran model was developed to iteratively alter the composition of Ti and Nb in each phase away from the initial bulk value and output the corresponding volume fraction of ω_{iso} for each value of $\phi(\Delta\rho)^2$ for all thermal exposure times. A graph of this iterative approach is shown in Figure 11, plotting the difference in atomic fraction of Nb between phases and the corresponding model prediction of ω_{iso} volume fraction for each thermal exposure. It was observed that conservation of matter and realistic volume fractions (based on earlier TEM observations) are only obtained by continuously increasing $n_{\text{Nb},\beta} - n_{\text{Nb},\omega}$ with increasing thermal exposure times. It also appears from this plot that the depletion of Nb in the ω_{iso} phase ($n_{\text{Nb},\beta} - n_{\text{Nb},\omega}$) and the volume fraction of ω are both far greater in the cold-rolled material than the as-extruded material. It is reasonable to believe that the actual values of $n_{\text{Nb},\beta} - n_{\text{Nb},\omega}$ and ω_{iso} volume fraction lie in the regions of highest slope, where there is a balance between sensible values for each term. For the 12.5 h AE condition, this corresponds to approximately $n_{\text{Nb},\beta} - n_{\text{Nb},\omega} = 7$– 11 at.%, $\phi_\omega = 7$ – 20%, and $n_{\text{Nb},\beta} - n_{\text{Nb},\omega} = 17$– 26 at.%, $\phi_\omega = 22$–50% for the 16 h CR condition. For the case of the CR material this is not conclusive as the nanoscale α may be contributing to the SANS measurement.

There are two possible methods that could be pursued in order to deduce the volume fraction from this experiment more accurately. The first is to perform atom-probe measurements on AE and CR Gum metal with different HT times at 400°C. This would measure the composi-

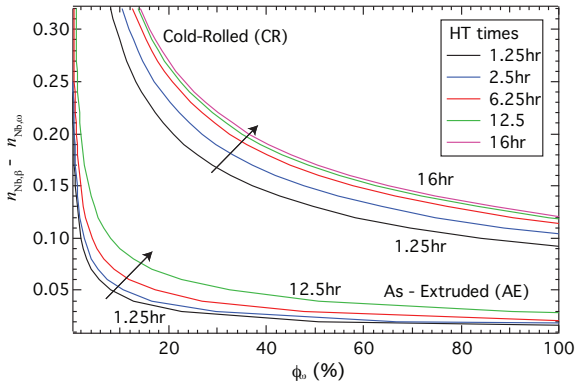

Figure 11: Variation of fitted ω molar fractions ϕ_ω with difference of Nb at.% between matrix and precipitate at different thermal exposures for the as-extruded (AE) and cold-rolled (CR) material, deduced from values of $\phi(\Delta\rho)^2$.

tion evolution in each phase due to the thermal exposure. However this technique is very localised, and may not necessarily be representative of the overall alloy. The second is to perform interrupted Small Angle X-Ray Scattering (SAXS) measurements, and by comparison of the SAXS and SANS data, one may be able to determine a value for $\Delta\rho$ [42]. Both of these are beyond the scope of the current paper.

It is interesting to note that the evolution of the $\phi(\Delta\rho)^2$ term for the cold-rolled and as-extruded sample (Figure 10) show similarities to the hardness measurements trendlines (Figure 1). The micro-hardness of the as-extruded sample increases quite linearly $\sim 250 - 280$Hv between $0 - 12.5$ h, while the cold-rolled micro-hardness increases quite dramatically from $\sim 280 - 400$Hv in the first 6 h, after which it plateaus. Thus, the large increase in the CR micro-hardness may correspond to the large increase in the $\phi(\Delta\rho)^2$ CR term, while a small increase in AE micro-hardness may correspond to the small increase in the $\phi(\Delta\rho)^2$ AE term. Jones *et al.* [17] suggest that ω leads to the rapid formation of fine scale α precipitates and a resulting increase in hardness. This work suggests that, although fine scale α is present in the cold-rolled material (Figures 5), the rapid increase in hardness may be due to rapid isothermal ω formation at 400°C, in agreement with Ikeda [43].

5. Conclusions

An *in-situ* SANS measurement studying phase nucleation and growth in a Ti alloy during thermal exposure has been successfully performed for the first time at the GP-SANS at ORNL HFIR. Specimens of Gum metal with different processing routes were studied, one specimen was as-extruded, the other was as-extruded followed by 90% cold-rolled. The processing route is shown to dramatically alter particle evolution during thermal exposure at 400°C.

Streaking along the $\{112\}_\beta$ on the $<110>_\beta$ zone axis shows that athermal ω was initially present in both samples, (Figure 3). The intensity was greater in the cold-rolled material, suggesting the athermal phase is induced during deformation.

Ex-situ TEM studies illustrate that isothermal ω was present after just 0.25 h in the cold-rolled material when heat-treated at 400°C. The evolution of ω_{ath} to ω_{iso} was much slower in the as-extruded material than the cold-rolled material. Dark-field TEM imaging suggested that the α may nucleate from isothermal ω in this material, as previously suggested by Nag *et al.* [15, 16].

In TEM, it was found that ω particles were localised in regions of certain grains for all conditions in the as-extruded material, whereas they were well distributed through all grains in the cold-rolled material.

XRD shows clear peaks from the ω phase in both samples following the longest time thermal exposures.

The room temperature SANS measurements of both samples showed no strong scattering from fine particles. This reinforces the argument that athermal ω has the same composition as the β phase, as a neutron scattering contrast due to different element distributions in each phase is required for neutron scattering.

During thermal exposure at 400°C the precipitation of the scattering phase was far more rapid in the cold-rolled sample than the as-extruded. From SANS modelling and based upon TEM it is suggested that the scattering phase was isothermal ω for the extruded material, with disc-shaped particles. It is not possible to conclusively state the scattering is arising from the ω phase alone in the cold-rolled data due to co-precipitation of the α phase, however based upon TEM diffraction patterns the authors believe scattering is predominantly from ω. The $\phi(\Delta\rho)^2$ term increased very rapidly in the first 4 h of thermal exposure and then plateaued for the cold-rolled material, while the precipitation process was more linear in the as-extruded sample over the first 12 h. The rapid evolution of the SANS $\phi(\Delta\rho)^2$ term of the cold-rolled sample, when compared to the as-extruded sample, is most likely due to a greater initial presence of athermal ω and/or a higher dislocation density.

The scattering intensity is very sensitive to the distribution of Ti and Nb in the alloy. With modelling it is shown that the ω_{iso} volume fraction in the cold-rolled + heat-treated material was far greater than the equivalent as-extruded material, and that it was also far more depleted in Nb. This is supported by the higher intensities in the ω TEM diffraction spots in the cold-rolled material. Sensible limits are suggested for the range of volume fraction and Nb partitioning for both processing conditions.

The rapid isothermal ω precipitation occurring in the cold-rolled sample corresponded to a significant improvement in hardness, from 280Hv to 400Hv in 6 h.

Acknowledgements

JC, VV, NGJ and DD would like to acknowledge funding from EPSRC under grant EP/H0004882/01. JC and MO would also like to acknowledge fellowship funding provided by JSPS. This work utilizes the Oak Ridge National Laboratory's High Flux Isotope Reactor, which is sponsored by the Scientific User Facilities Division, Office of Basic Energy Sciences, U.S. Department of Energy. We would like to thank Matthias Knop at Imperial, Mark Ward at the University of Birmingham and Richard Dashwood at Warwick University for their help with sample manufacture and preparation.

References

[1] Saito T *et al.* Science 2003;300:464
[2] Boyer RR, Briggs RD. J Mater Eng Perform 2005 14:681
[3] Raghunathan SL, Stapleton AM, Dashwood RJ, Jackson M, Dye D. Acta Mater 2007 55:6861
[4] Nag S, Banerjee R, Fraser HL. J Mater Sci 2005 16:679
[5] Banerjee S, Tewari R, Dew GK. Int J Mater Sci 2006 97:963
[6] Ramsteiner *et al.* Acta Mater 2008 56(6):1298
[7] Duerig TW, Williams JC. In: Boyer RR, Rosenberg HW, eds., AIME, New York, USA, 1984:19–67

[8] Nag S *et al.* Phy Rev Lett 2011 106:245701
[9] Jones NG, Dashwood RJ, Jackson M, Dye D. Acta Mater 2009 57:3830
[10] Furuta T *et al.* In: Lutjering G, ALbrecht J, eds., Ti–2003 Science and Technology, WILEY-VCH, Weinheim, Germany, 2004:1519–1526
[11] Collins DM, Heenan RK, Stone HJ. Metal Mater Trans A 2011 42:49
[12] Miller RJR, Messoloras S, Stewart RJ, Kostorz G. J Appl Cryst 1978 11:583
[13] Veron M, Bastile P Acta Mater 1997 45:3277
[14] Strunz P, Mukherji D, Gilles R, Wiedenmann A, Roesler J Fuess H J Appl Cryst 34:541
[15] Nag S, Banerjee R, Fraser HL. J Mater Sci 2009;44:808
[16] Nag S, Banerjee R, Srinivasan R, Hwang JY, Harper M, Fraser HL. Acta Mater 2009 57:2136
[17] Jones NG, Talling RJ, Lindley TC, Dye D. In: L Zhou *et al.* eds., Ti2011 Science and Technology: Proceedings of the 12th World Conference on Titanium. Science Press, Beijing, China. 2012:1169–1173
[18] Talling RJ, Dashwood RJ, Jackson M, Dye D. Acta Mater 2009 57:1188
[19] Obbard EG, Hao YL, Akahori T, Talling RJ, Niinomi M, Dye D, Yang R. Acta Mater 201058:3557
[20] Coakley J, Reed RC, Warwick JLW, Rahman KM, Dye D. Acta Mater 2012;60:2729
[21] Stone HJ, Holden TM, Reed RC. Acta Metall 1999;47:4435
[22] Ma S, Rangaswamy P, Majumdar BS. Scr Mater 2003;48:525
[23] Ma S, Brown D, Bourke MAM, Daymond MR, Majumdar BS. Mater Sci Eng A 2005;399:141
[24] Daymond MR, Preuss M, Clausen B. Acta Mater 2007;55:3089
[25] Preuss M, da Fonesca JQ, Grant B, Knoche E, Moat R, Daymond M. In: Reed RC, Green KA, Caron P, Gabb TP, Fahrmann MG, Huron ES, Woodard SA, eds., Superalloys 2008. TMS, PA, 405–414
[26] Dye D, Coakley J, Vorontsov VA, Stone HJ, Rogge RB. Scr Mater 2009;48:525
[27] Coakley J, Dye D. Scri Mater 2012;67:435
[28] Wignall GD, Littrell KC, Hetter WT, Melnichenko YB, Kailey KM, Lynn GW, Myles DA, Urban VS, Buchanan MV, Selby DL, Bulter PD J Appl Cryst 2012;45:990
[29] Hull AW Phys Rev 1921;18:88
[30] Wyckoff RWG In: Crystal structures. 2nd Edition, Vol. 3, Interscience Publishers, New York, New York, 1963:7–83
[31] Jamieson JC Science 1963;140:72
[32] Warwick J.L.W, Coakley J, Raghunathan S.L, Talling R.J, Dye D. Acta Mater 2012;60:4117
[33] Kline SRJ. J Appl Cryst 2006;39(6):895
[34] Heenan RK. RAL Report 1989;89
[35] Alina G, Butler P, Cho J, Doucet M, Kienzle P. "SAS analysis software", *to be published.*
[36] King SM. In: Pethrick RA, Dawkins JV, eds., Modern techniques for polymer characterisation. Wiley, Chichester, 1999:171–232
[37] van de Hulst HC. Light Scattering by Small Particles. Wiley, 1957
[38] Livsey I. J Chem Soc., Faraday Trans. 2 1987;83(8):1445
[39] Ashcroft NW, Lekner J. Phys Rev 1966;145:83
[40] Porod G. Kolloiz-Z 1951;124:83
[41] Sears VF. Neutron News 1992;(3)3:26
[42] Ohnuma M, Suzuki J, Ohtsuka S, Kim S.-W, Kaito T, Inoue M, Kitazawa H. Acta Mater 2009;(3)57:5571
[43] Ikeda M, Ueda M, matsunaga R, Ogawa M, Niinomi M. Mater Trans 2009;(50)12:2737